



A Split-Gate Positive Feedback Device With an Integrate-and-Fire Capability for a High-Density Low-Power Neuron Circuit

Kyu-Bong Choi, Sung Yun Woo, Won-Mook Kang, Soochang Lee, Chul-Heung Kim, Jong-Ho Bae, Suhwan Lim and Jong-Ho Lee*

Department of Electrical and Computer Engineering, Inter-University Semiconductor Research Center, Seoul National University, Seoul, South Korea

OPEN ACCESS

Edited by:

Arindam Basu,
Nanyang Technological University,
Singapore

Reviewed by:

Shreyas Sen,
Purdue University, United States
Anh Tuan Do,
Institute of Microelectronics (A*STAR),
Singapore
Nripan Mathews,
Nanyang Technological University,
Singapore

*Correspondence:

Jong-Ho Lee
jhl@snu.ac.kr

Specialty section:

This article was submitted to
Neuromorphic Engineering,
a section of the journal
Frontiers in Neuroscience

Received: 05 June 2018

Accepted: 18 September 2018

Published: 09 October 2018

Citation:

Choi K-B, Woo SY, Kang W-M,
Lee S, Kim C-H, Bae J-H, Lim S and
Lee J-H (2018) A Split-Gate Positive
Feedback Device With an
Integrate-and-Fire Capability
for a High-Density Low-Power Neuron
Circuit. *Front. Neurosci.* 12:704.
doi: 10.3389/fnins.2018.00704

Hardware-based spiking neural networks (SNNs) to mimic biological neurons have been reported. However, conventional neuron circuits in SNNs have a large area and high power consumption. In this work, a split-gate floating-body positive feedback (PF) device with a charge trapping capability is proposed as a new neuron device that imitates the integrate-and-fire function. Because of the PF characteristic, the subthreshold swing (SS) of the device is less than 0.04 mV/dec. The super-steep SS of the device leads to a low energy consumption of ~ 0.25 pJ/spike for a neuron circuit (PF neuron) with the PF device, which is ~ 100 times smaller than that of a conventional neuron circuit. The charge storage properties of the device mimic the integrate function of biological neurons without a large membrane capacitor, reducing the PF neuron area by about 17 times compared to that of a conventional neuron. We demonstrate the successful operation of a dense multiple PF neuron system with reset and lateral inhibition using a common self-controller in a neuron layer through simulation. With the multiple PF neuron system and the synapse array, on-line unsupervised pattern learning and recognition are successfully performed to demonstrate the feasibility of our PF device in a neural network.

Keywords: neuromorphic, positive feedback, steep subthreshold swing (SS), integrate-and-fire (I&F), spiking neural network (SNN), unsupervised learning, pattern recognition

INTRODUCTION

Conventional computing systems based on von-Neumann architecture suffer from an energy efficiency problem compared to biological brains in processing the complex data and information (Cantley et al., 2011; Indiveri et al., 2011; Yu et al., 2011; Park et al., 2013). As an alternative to conventional computing architectures, neuromorphic computing architectures have been studied to enable complex processes, such as pattern recognition, classification, and perception (Wijekoon and Dudek, 2008; Ghosh-Dastidar and Adeli, 2009; Basu et al., 2013; Rajendran et al., 2013; Kasabov, 2014; Eryilmaz et al., 2015). Among these architectures, deep neural networks (DNNs) such as deep-belief network (DBN) and convolutional network (ConvNet), which are computing architectures that use a mathematical algorithm model, have been widely reported to reduce the computing energy by mimicking the parallel computation of biological brains (Hinton et al., 2006;

Turaga et al., 2010; LeCun et al., 2015; Krizhevsky et al., 2017; Liu et al., 2017). However, software-based DNNs still have energy efficiency issues due to the energy consumed by the synchronous information processing and data movement between the processor and memory such as static random access memory (SRAM) and dynamic random access memory (DRAM) (Chen et al., 2017). On the other hand, spiking neural networks (SNNs) based on event-driven sparse communication and local learning without using external memory can reduce the power consumption, and many studies have been reported (Kim et al., 2015; Moon et al., 2015; Qiao et al., 2015; Park and Lee, 2017). The SNNs mimic the human brain more closely, consisting of synapses and neurons, and provide a highly compact model for building a larger-scale neuromorphic system platform. The function of the “integrate-and-fire (I&F) neuron model,” which is the fundamental part of the SNNs, is that a neuron fires when integrated signals exceed a specific threshold. To implement a hardware-based I&F function in SNNs, various types of neuron circuits such as a log-domain LPF neuron, differential pair integrator and fully digital I&F circuit have been widely reported (Indiveri et al., 2011). However, complementary metal-oxide semiconductor (CMOS) based neuron circuits for complex neuron functions require many transistors and large capacitors including a membrane capacitor (C_{mem}) in a neuron circuit leading to a large area. Therefore, to implement a high density SNN, neuron devices with the integration capability have recently been reported, such as impact-ionization based NPN selector (I-NPN) and NPN device with an extended gate (gated-INPN) on a silicon-on-insulator (SOI) platform (Ostwal et al., 2015; Dutta et al., 2017), spin-transfer torque (STT) devices based on a magnetic tunnel junction (MTJ) (Sharad et al., 2012; Zhang et al., 2016) and memristor (Wang et al., 2018). However, the neuron circuit based on the SOI devices using the impact-ionization has the body-floated CMOS FETs, and their performance can be degraded by the floating-body effect (Vandana, 2013). The stochastic switching characteristic of the STT device can cause unwanted fires in neurons with integrated signals that do not exceed the threshold, and most of the materials that make up the device are not compatible with the CMOS process. The memristor is compatible with the CMOS process, but it has reliability issues when manufactured in a nanoscale and constructed as multiple array layers (Pouyan et al., 2014).

In addition, to achieve a low power neuron circuit, a device with steep switching characteristics is required. The switching characteristic of conventional MOSFETs is limited by the theoretical limit of the subthreshold swing (SS) of 60 mV/dec at room temperature ($T = 300$ K) (Cheung, 2010). To overcome the switching limitation of conventional MOSFETs, many steep SS devices have been reported, such as an impact-ionization MOS (I-MOS) using the avalanche break down (Choi et al., 2005), band-to-band tunneling FET (TFET) (Choi et al., 2007) and PNP based-feedback FETs (FB-FETs) (Wan et al., 2013; Jeon et al., 2015; Dirani et al., 2017). These steep SS devices are fabricated using SOI wafers because they require a floating-body to reduce leakage or to accumulate carriers. However, the performance of body-floated CMOS FETs fabricated on a SOI wafer with steep SS device can be degraded

by the floating-body effect and self-heating effect (Su et al., 1994).

In this paper, we propose, for the first time, a split-gate floating-body positive feedback (PF) device based on a gated PNP structure for the I&F function and introduce key fabrication steps for the PF device fabricated using the CMOS process. For an I&F neuron circuit, body-connected CMOS FETs are fabricated on the same wafer with a body-floated PF device. The fabricated devices are investigated in terms of the fundamental device properties and neuron operation. With the PF device, we also demonstrate the I&F, reset and lateral inhibition functions of the SNN system using a circuit simulator and performed on-line unsupervised pattern learning and recognition using a MATLAB simulator.

MATERIALS AND METHODS

Device Fabrication and Integration

The PF device and several CMOS FETs were fabricated on the same (100) bulk Si wafer using 11 masks and unit processes of the CMOS technology. **Figure 1** shows schematic cross-sectional views of key process steps for the PF device, the split-gate floating-body FET, and the split-gate bulk FET, the single-gate floating-body FET and the single-gate bulk FET. A thin sacrificial silicon dioxide (SiO_2) was deposited and patterned. A thin silicon nitride (Si_3N_4) was deposited to passivate the sacrificial SiO_2 . Then, a thick poly-Si layer was deposited and patterned (**Figure 1A**), followed by Si_3N_4 deposition and etching for the spacer formation (**Figure 1B**). The poly-Si was stripped, and the $\text{SiO}_2/\text{Si}_3\text{N}_4$ not protected by the Si_3N_4 spacer was etched (**Figure 1C**). Through these process steps, the Si_3N_4 spacers with and without the sacrificial SiO_2 were formed for the split-gates and single-gate formation on the same wafer. Si fins were formed by dry etching using the Si_3N_4 spacer as a hard-mask (**Figure 1D**). After forming the SiO_2 /amorphous silicon (a-Si) (25 nm/25 nm) stack (**Figure 1E**), only the a-Si was patterned to form sidewall masks with different thicknesses using a photoresist (PR) mask (**Figure 1F**). Then, the SiO_2 and the SiO_2 /a-Si stack were anisotropically etched followed by isotropic etching of the exposed Si (**Figures 1G,H**). Note that only the Si fins with thinner sidewall masks were floated by controlling the etching time with SF_6 gas leading to the formation of the floating fin and bulk fin bodies on the same substrate. By wet etching all of the SiO_2 in a buffered hydrogen fluoride (BHF) solution, the SiO_2 sidewall masks and only the Si_3N_4 spacers formed on the sacrificial SiO_2 were removed (**Figure 1I**). A thick SiO_2 layer was deposited by a high-density plasma chemical vapor deposition (HDP-CVD) process and wet etched partly to form an isolation oxide (**Figures 1J,K**). A thin SiO_2 buffer layer was deposited to protect against ion implant damage followed by ion implantations for the control of the threshold voltage under the isolation oxide, electron injection barrier (p-type doping, Np), and n-/p-well doping. After removing the buffer SiO_2 , a tunneling $\text{SiO}_2/\text{Si}_3\text{N}_4$ /blocking SiO_2 (O/N/O) gate insulator stack was formed for the charge trap layer, and a heavily doped n-type (n+) polysilicon (poly-Si) was deposited for the gate

formation. By coating the wafer with a thinned PR (2:1 mixture of PR and thinner), the PR on the n+ poly-Si deposited on the Si₃N₄ spacers was much thinner than that on the n+ poly-Si without the Si₃N₄ spacers (**Figure 1L**). After partly etching the thinly coated PR, only the n+ poly-Si on the Si₃N₄ spacers was exposed (**Figure 1M**). Then, the exposed n+ poly-Si was etched partly to split the n+ poly-Si on both sides of the Si₃N₄ spacer (**Figure 1N**). Then, the thinned PR was removed followed by the n+ poly-Si patterning to form the gates (**Figure 1O**). The split-gates and single-gates were formed on the same wafer. The O/N/O stack and the Si₃N₄ spacer in the ungated region were removed. After a buffer SiO₂ was grown on the Si fins, ion implantations were performed for the source/drain (S/D) or anode/cathode and hole injection barrier doping (n-type doping, Nn). This was followed by a rapid thermal annealing (RTA) at

a temperature of 1050°C for 5 s. Then, an inter-layer dielectric (ILD) was deposited, and contact holes were patterned. A nickel (Ni)/titanium nitride (TiN) stack was deposited, and silicidation was performed by annealing at a temperature of 450°C for 1 min for NiSi formation (Wu et al., 2007). After unreacted Ni and TiN were stripped in piranha solution (H₂SO₄/H₂O₂), TiN was deposited and patterned for the electrode followed by H₂ annealing at 350°C for 10 min.

Electrical Characterization

Electrical characterization of the fabricated PF device and the four different kinds of devices was carried out using a probe station (Cascade, Cascade Microtech), a semiconductor device analyzer (B1500A, Agilent Technologies) and a waveform generator and fast measurement unit (WGFMU) module. Simulated I–V curves

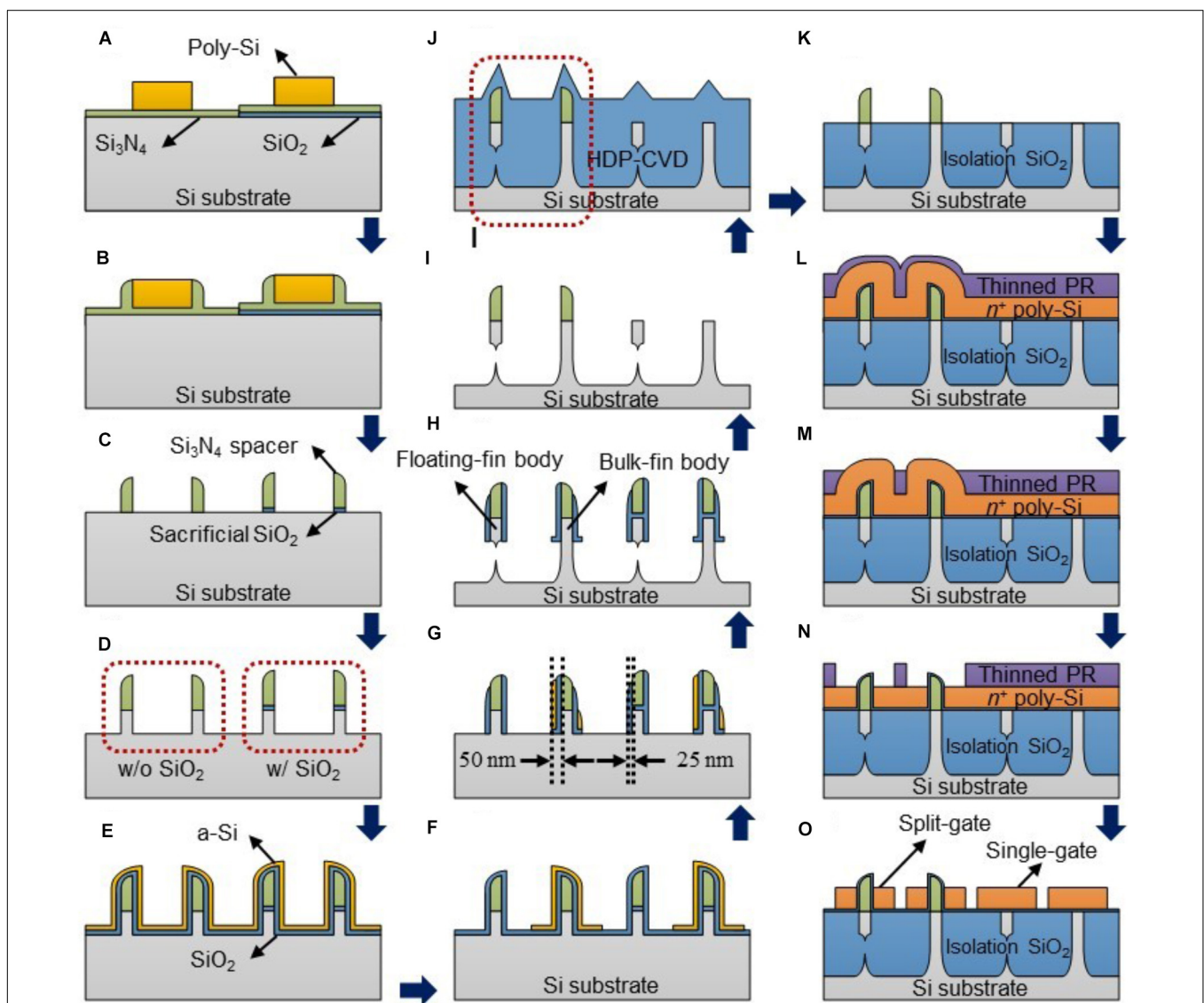


FIGURE 1 | (A–O) Schematic cross-sectional views of key process steps of the fabricated positive feedback (PF) device or the split-gate floating-body FET (leftmost in each figure), the split-gate bulk FET, the single-gate floating-body FET and the single-gate bulk FET (sequentially from the left in each figure) on the same substrate.

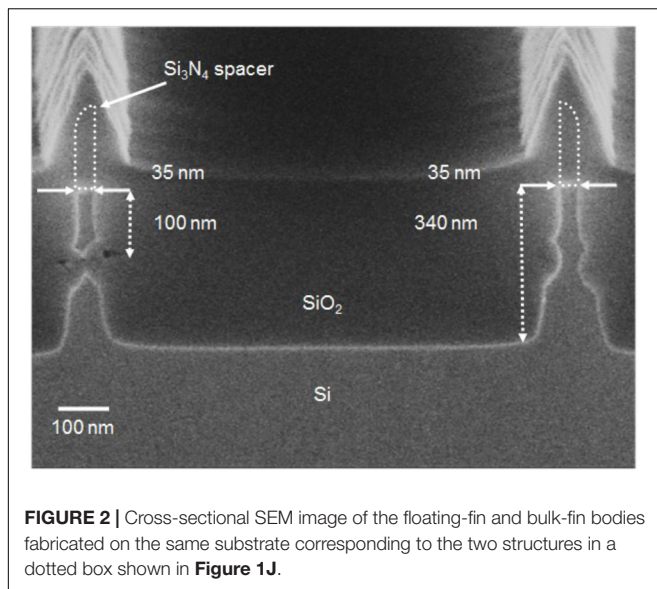


FIGURE 2 | Cross-sectional SEM image of the floating-fin and bulk-fin bodies fabricated on the same substrate corresponding to the two structures in a dotted box shown in **Figure 1J**.

and energy band diagrams were obtained from a TCAD simulator (Sentaurus, Synopsys).

I&F Circuit and Multiple Neuron System

The I&F circuit with the PF device was simulated using a TCAD mixed-mode simulator (Sentaurus, Synopsys). In the mixed-mode simulations, the PF device was simulated by a device simulator, and the several CMOS FETs were simulated by a circuit simulator. The multiple neuron system including the PF neuron circuits, which have several CMOS FETs and an equivalent circuit reflecting the electrical behavior of the fabricated PF device, was simulated using a circuit simulator (HSPICE, Synopsys) with Predictive Technology Models (PTMs).

Pattern Classification

The pattern classification was evaluated through simulations using the MATLAB software. The fully connected 2-layer SNN system was used to perform system-level verification of the pattern classification. The system consists of an input layer of 784 presynaptic neurons and an output layer of 10 postsynaptic neurons. The pattern classification was carried out in two steps: learning and recognition. Before the learning process, the weights of all the synapses were initialized to a random distribution. In the learning process, the synchronized binary 28×28 input pulses were applied to the synapse array. The behavioral modeling of synaptic devices and the proposed spike-timing-dependent plasticity (STDP) learning rule (Kim et al., 2018) were used for learning the synaptic weights. The I&F, reset and lateral inhibition functions were used for systematic operation of multiple neurons. In the recognition process, the I&F and reset functions were only used, and the firing rates of 10 output neurons were compared to identify which number is recognized.

RESULTS AND DISCUSSION

Key Feature of the PF Device

The PF device with steep switching characteristics using PF requires a floating-body channel to accumulate the injected electrons and holes to lower the hole and electron injection barriers, respectively. However, when neuron circuits including PF devices are integrated on the same substrate with CMOS FETs, these FETs have a floating-body, which may degrade the performance of the device. Therefore, a new process design should be made to enable the floating-body and the body connected to the substrate to be implemented on the same wafer. We successfully fabricated body-floated (floating-fin body) PF devices and body-connected (bulk-fin body) CMOS FETs on the same wafer (see section “Materials and Methods”). **Figure 2** shows a cross-sectional scanning electron microscopy (SEM) image of the floating-fin and bulk-fin bodies fabricated on the same substrate corresponding to the two structures in the dotted box shown in **Figure 1J**. I - V characteristics of the bulk-fin body CMOS FETs and several devices fabricated on the same wafer are shown in **Supplementary Figure S1**.

Figures 3B,C show the top and three-dimensional schematic views of the proposed PF device corresponding to part of the biological neuron depicted by the dotted box in **Figure 3A**. The PF device based on a gated PNP structure has an anode, ungated region (n -type, hole injection barrier), gated region (p -type, electron injection barrier) and cathode region sequentially from the left shown in **Figure 3C**. Both the anode (p^+) and cathode (n^+) doping concentrations (or source/drain of the p -MOSFET and n -MOSFET, respectively) of the fabricated PF device are $2 \times 10^{20} \text{ cm}^{-3}$ for the ohmic contact between the TiN and the doped regions. The doping concentration of both hole and electron injection barriers is $\sim 1 \times 10^{18} \text{ cm}^{-3}$. **Figure 3D** shows a cross-sectional transmission electron microscopy (TEM) image of the fabricated PF device cut along the dashed line A-A' in **Figure 3C**. The PF device has a split-gate floating-body structure. The n^+ poly-Si gate1 (G1) and gate2 (G2) are located on both sides of the Si_3N_4 spacer. The floating-fin body width (W_{fin}) and height (H_{fin}) are 35 nm and 100 nm, respectively. The thickness of the O/N/O stack between the channel and gate for the charge trap layer is 2/4.2/9 nm. Here, the overlap height (H_G) between the gate and Si fin is very small. The turn-on voltage (V_{on}) of the PF device at which the anode current (I_A) suddenly increases is weakly dependent on the H_G shown in **Figure 4**. Note that the H_G very slightly affects the V_{on} at a G2 bias (V_{G2}) lower than -1 V . Thus, we adopted a H_G of 0 nm (nearly planar channel) to demonstrate the key concept of our PF device.

I - V Characteristics of the Proposed PF Device

Figure 5A shows the I_A versus G1 bias (V_{G1}) curve of the fabricated PF device at a V_{G2} of 2 V and an anode bias (V_A) of 1 V. The length of both the electron (L_p) and hole (L_n) injection barriers is 1 μm . The SS of the PF device is less than 0.04 mV/dec (resolution limit of the measurement system) shown in the inset of **Figure 5A**. As far as we know, the proposed PF device has

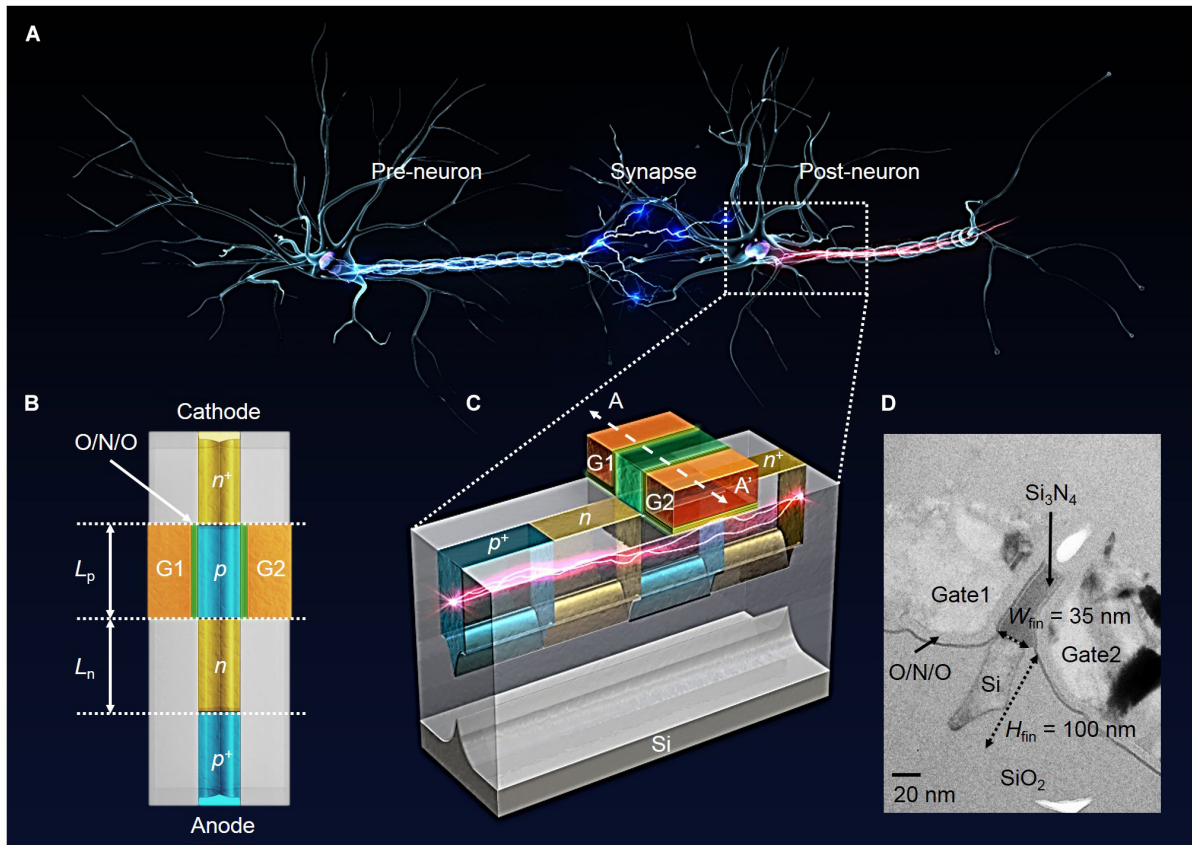


FIGURE 3 | Schematic and cross-sectional views of the fabricated PF devices. **(A)** Three-dimensional illustration of biological neurons. **(B)** Top view of the PF device. **(C)** Three-dimensional schematic view of the fabricated PF device as a neuron device to mimic the I&F function of biological neurons. **(D)** Cross-sectional TEM image of the fabricated PF device cut along the dashed line A–A’ in **(C)**. Here, the width and height of the floating-fin body are 35 and 100 nm, respectively.

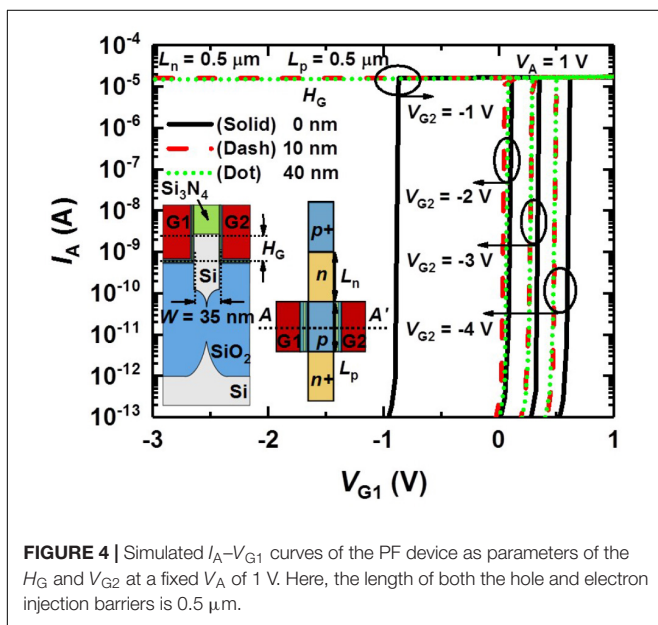
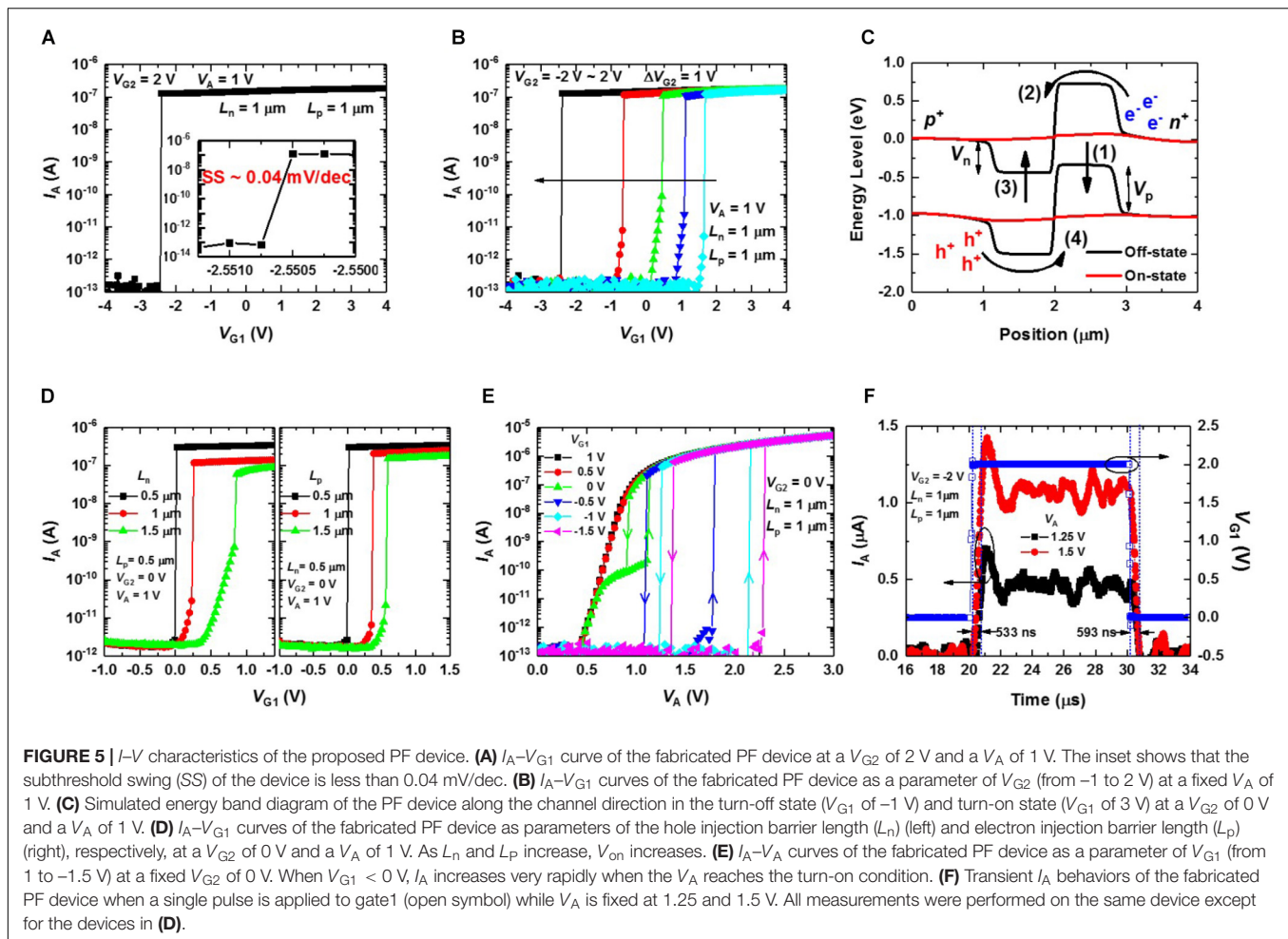


FIGURE 4 | Simulated I_A – V_{G1} curves of the PF device as parameters of the H_G and V_{G2} at a fixed V_A of 1 V. Here, the length of both the hole and electron injection barriers is 0.5 μm .

the smallest SS compared to the other step SS devices reported (Table 1). Additionally, V_{on} of the PF device can be modulated by the V_{G2} (Figure 5B). The abrupt increase of the current is due to the PF triggered by the applied V_{G1} . The mechanism of the steep switching operation can be explained by an energy band diagram. Figure 5C shows the simulated energy band-diagram of the PF device along the channel in the turn-off state (V_{G1} of -1 V) and turn-on state (V_{G1} of 3 V) at a V_{G2} of 0 V and a V_A of 1 V. As the V_{G1} is increased, the electron injection barrier (V_p) decreases (1), and electrons are injected into the hole injection barrier region (2) which leads to a decrease of the hole injection barrier (V_n) (3). Then, the holes are injected into the electron injection barrier region (4) further reducing the V_p (1), and electrons are injected into the hole injection barrier region again. As this process repeats with PF, the device switches rapidly from the turn-off state to the turn-on state. However, as the L_n or L_p increases, the recombination of minority carriers increases leading to an increase of V_{on} , a decrease of I_{on} , and the degradation of the sharp switching characteristic (Figure 5D).

Figure 5E shows the I_A – V_A curves as a parameter of V_{G1} at a fixed V_{G2} of 0 V. When $V_{G1} > 0$ V, I_A shows p - n diode properties because V_p is effectively decreased by the positively biased V_{G1} . When $V_{G1} < 0$ V, I_A shows rapid switching due to



the PF being triggered by the carriers generated in the reversed biased p - n junction as V_A increases. The generated holes and electrons accumulate in the electron and hole injection barrier regions, respectively, which leads to the decrease of V_p and V_n . Then, electrons and holes are injected into the hole and electron injection barrier regions, respectively, to further reduce the V_n and V_p . As this process repeats, the I_A shows sharp switching characteristics in the forward V_A scan. Hysteresis occurs when the reverse V_A scan time is shorter than the lifetime of the injected minority carriers after abrupt switching occurs in the forward V_A scan. The transient I_A behaviors when V_{G1} is switched from 0 to 2 V and again to 0 V at a fixed V_{G2} of -2 V are shown in **Figure 5F**. We can clearly see the turn-on and turn-off characteristics in the figure.

We also demonstrate that the proposed PF device works at the 14 nm node by showing simulated I_A - V_{G1} curves (**Figure 6**). Here, the W_{fin} , H_{fin} , length (L_G) of gates (G1 ~ G4), and p -type doping concentration in the floating-fin body except for the anode and cathode are 10, 40, and 14 nm and $2 \times 10^{15} \text{ cm}^{-3}$, respectively. The gate stack formed between the gate and channel consists of SiO_2 (2 nm)/ Si_3N_4 (4 nm)/ SiO_2 (6 nm). When a V_{G2} of < -3 V, a V_{G3} of > 3 V, and a V_{G4} of > 3 V, I_A show rapid switching as V_{G1} increases. Note that the hole and

electron injection barriers (n -type and p -type) are formed by the appropriate biases ($V_{G2} \sim V_{G4}$).

I&F Function of the PF Device

Figure 7A compares the I - V curves of a fabricated single-gate bulk n FET and the PF device with the charge trap layer in the initial, program (PGM) and erase (ERS) states. Here, the W and L of the single-gate bulk n FET are 35 nm and 1 μm , respectively. Both L_n and L_p of the PF device are 1 μm . When the shift in V_{on} (V_{th}) of the PF device (the single-gate bulk n FET) between the PGM and ERS states is 0.5 V, the PF device has a much larger I_{on}/I_{off} ratio than that of the single-gate bulk n FET because of the super-steep SS property. **Figure 7B** shows the SS change of the fabricated single-gate bulk n FET and PF device as the PGM/ERS cycling increases from 1 to 10^5 . The SS of the PF device does not change while the SS of the single-gate bulk n FET increases from 95 to 160 mV/dec. Moreover, reasonable retention characteristics of the PF device at the PGM/ERS states are shown in **Figure 7B**. The charge trap function of the proposed PF device (12F^2) improves the integration density by replacing the integrate-function of the membrane capacitor (C_{mem}) which occupies a large area in conventional neuron circuits (Chicca

TABLE 1 | Comparison of the electrical characteristics of steep SS devices.

Reference	Substrate	Operating Principle	$ V_{DS} $ (V)	I_{on}/I_{off}	SS (mV/dec)
Choi et al., 2005	SOI	Avalanche breakdown	6.5	$\sim 10^6$	3.7
Abele et al., 2005	Bulk	Mechanical switching	8.9	$> 10^3$	2.16
Choi et al., 2007	SOI	Band-to-band tunneling	1	$\sim 10^4$	52.8
Jo et al., 2015	Bulk	Negative capacitance	2	$\sim 10^5$	18
Wan et al., 2012, 2013	SOI	Positive feedback	1.5	$\sim 10^8$	~ 1
Jeon et al., 2015	Flexible	Positive feedback	1	$\sim 10^6$	10
Dirani et al., 2016	SOI	Positive feedback	1-1.5	$\sim 10^{10}$	8
Dirani et al., 2017	SOI	Positive feedback	1.2	$\sim 10^8$	7
This work	Bulk	Positive feedback	1	$\sim 10^6$	~ 0.04

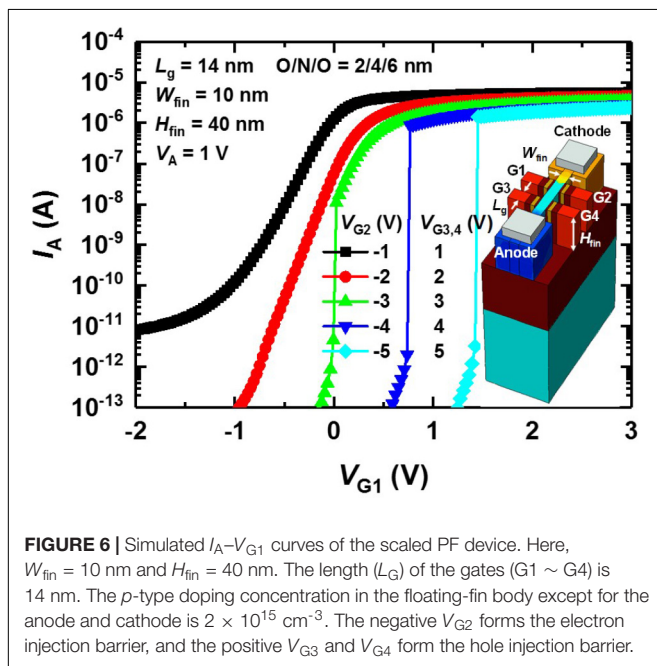


FIGURE 6 | Simulated I_A - V_{G1} curves of the scaled PF device. Here, $W_{fin} = 10$ nm and $H_{fin} = 40$ nm. The length (L_g) of the gates (G1 ~ G4) is 14 nm. The p -type doping concentration in the floating-fin body except for the anode and cathode is 2×10^{15} cm $^{-3}$. The negative V_{G2} forms the electron injection barrier, and the positive V_{G3} and V_{G4} form the hole injection barrier.

et al., 2014). A C_{mem} of 0.5 pF has a footprint of 100 μm^2 (816F 2) for a 0.35 μm CMOS process (Livi and Indiveri, 2009).

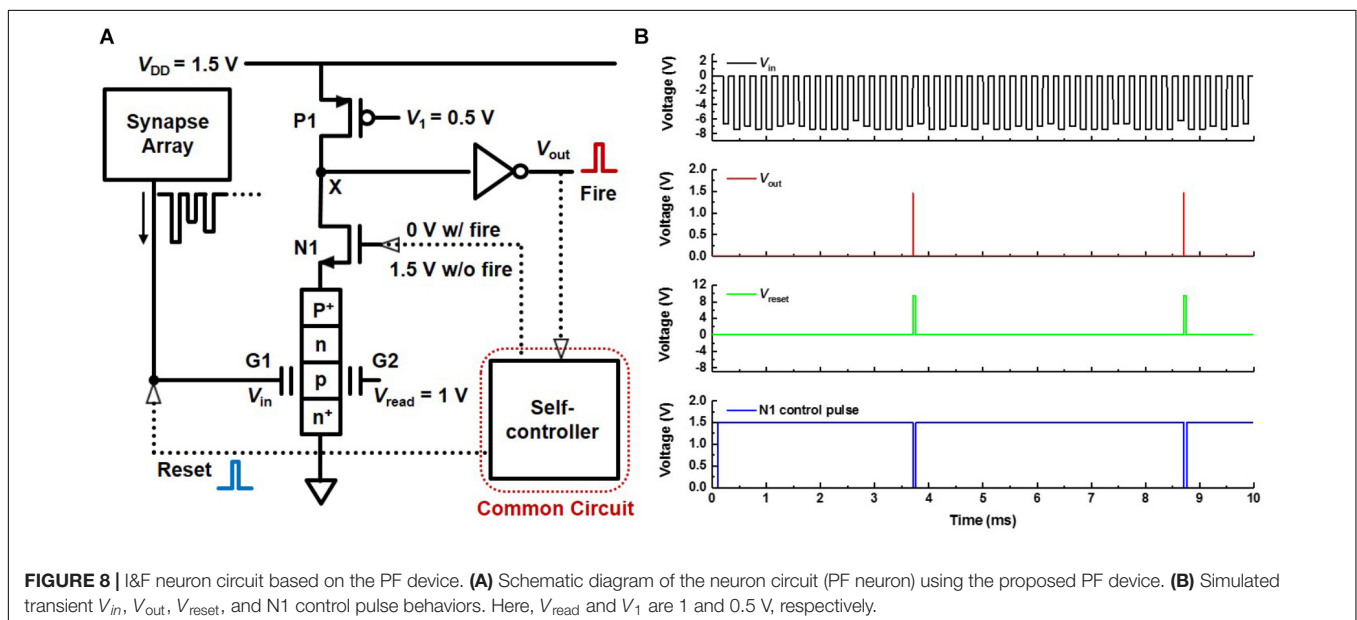
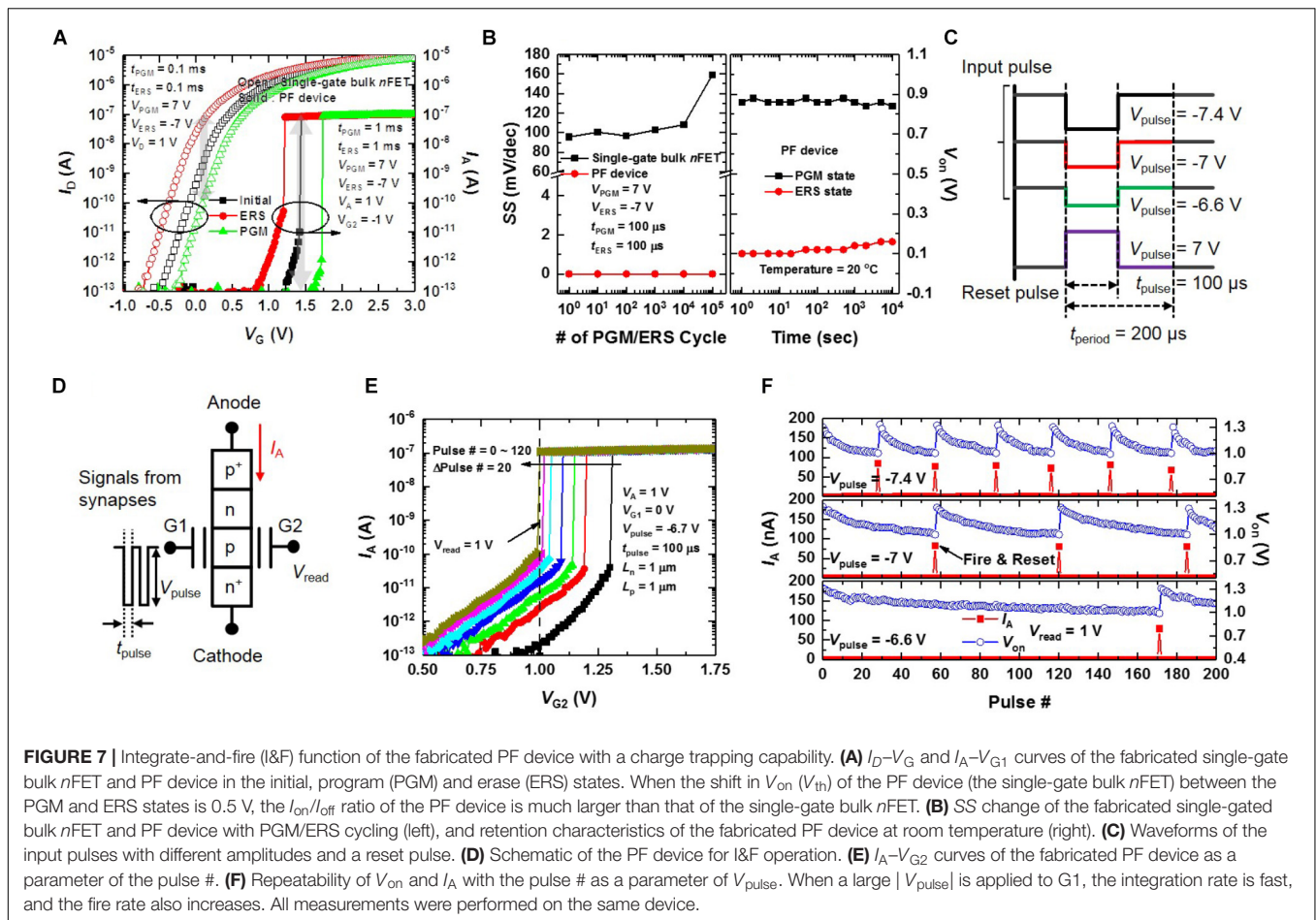
Figure 7E demonstrates the I&F function of our PF device by showing the I_A versus V_{G2} curves as a parameter of the number of pulses at a fixed V_A of 1 V. A pulse bias (V_{pulse}) of -6.7 V is applied to G1 at the read bias (V_{read}) applied to G2 of 1 V shown in **Figure 7D**. As the V_{pulse} is repeatedly applied to G1, trapped electrons in the charge trap layer are detrapped into the p -type Si (electron injection barrier). Then, V_{on} of the PF device decreases gradually. When the number of V_{pulse} exceeds 120, V_{on} becomes less than 1 V leading the device to switch quickly from the off-state to the on-state. Thus, the I&F function is verified in our PF device. **Figure 7F** shows the repeatability of V_{on} and I_A with

the number of pulses as a parameter of V_{pulse} (see **Figure 7C**) at a V_{read} of 1 V. When V_{on} is less than 1 V, the PF device fires. After firing, we reset V_{on} of the PF device by applying the reset pulse (see **Figure 7C**) to G1 to store electrons in the charge trap layer. As $|V_{pulse}|$ increases, the fire rate increases because more electrons are detrapped from the charge trap layer into the p -type Si at a larger $|V_{pulse}|$.

I&F Neuron Circuit Based on the PF Device

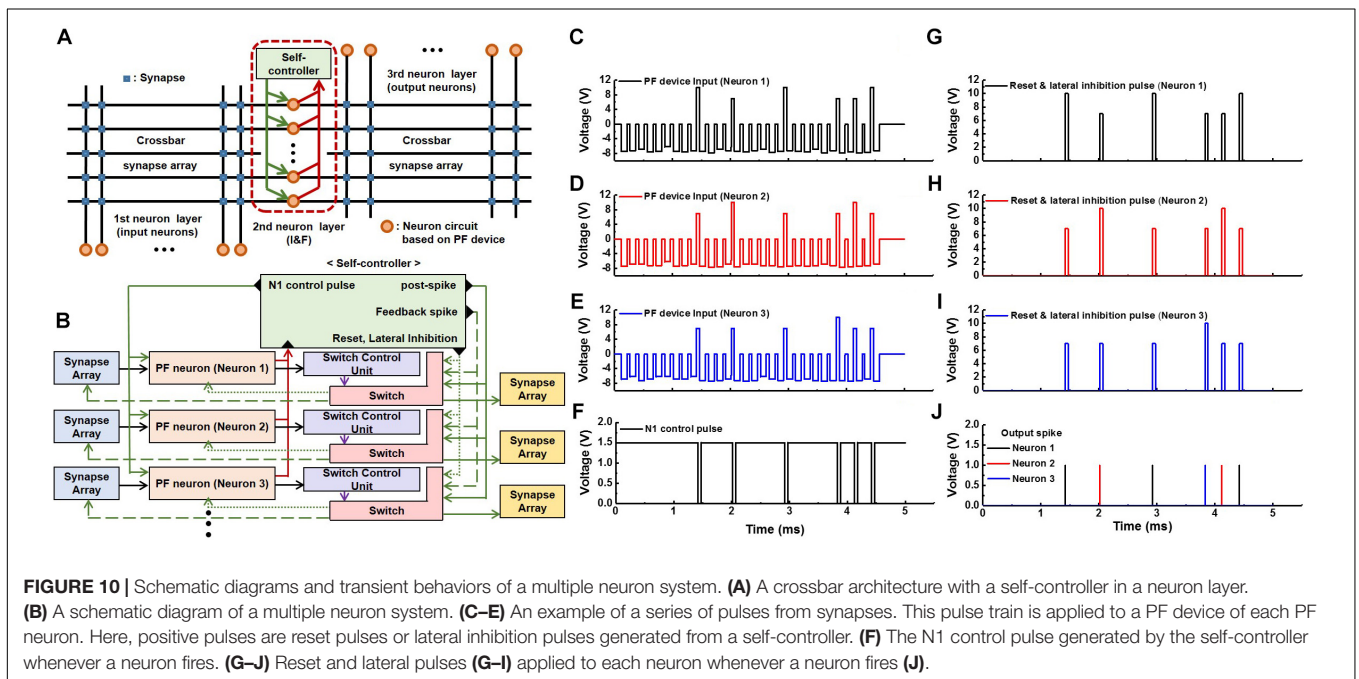
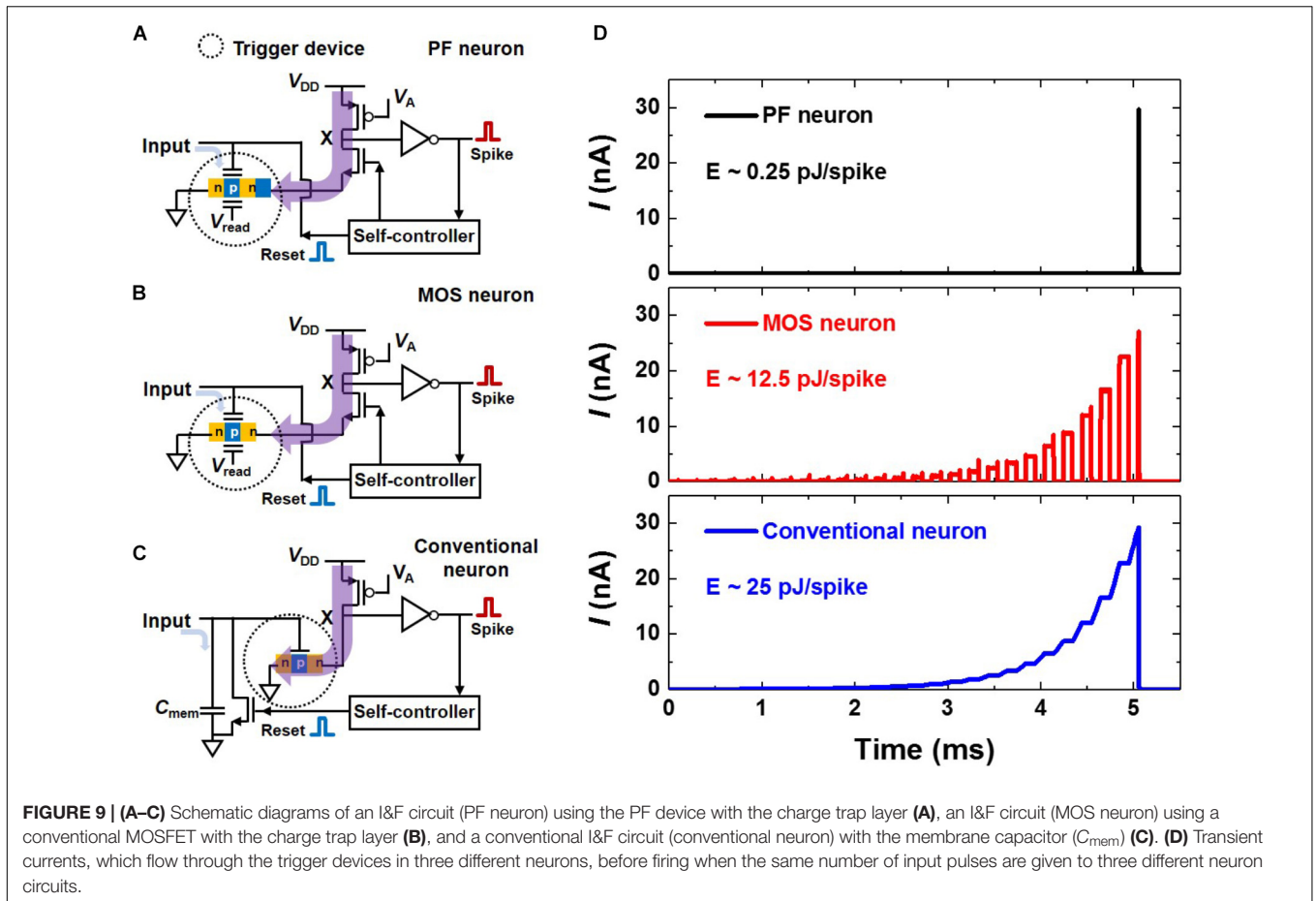
Figure 8A shows a schematic diagram of a neuron circuit (PF neuron) which includes the PF device. Here, the self-controller applies 0 V to the gate of the n -MOSFET (N1) when the neuron fires and 1.5 V otherwise. It also applies a reset pulse to the G1 of the PF device when the neuron fires. The operation scheme of the PF neuron is as follows. When signals are repeatedly transmitted from the synapses to the G1 of the PF device, they are integrated into the charge trap layer of the PF device, and the V_{on} of the PF device is gradually reduced. At the very moment V_{on} becomes lower than V_{read} , the PF device rapidly switches from the turn-off state to the turn-on state. Then, the voltage at node X changes from a high level to a low level leading to the neuron firing through the inverter. After the neuron fires, N1 is turned off, and the reset pulse is applied to the PF device by the self-controller to return the PF device to its initial state. The simulated transient V_{in} , V_{out} , V_{reset} , and N1 control pulse behaviors of the neuron circuit are shown in **Figure 8B**. These operations verify that the PF neuron mimics effectively the I&F function of the biological neuron.

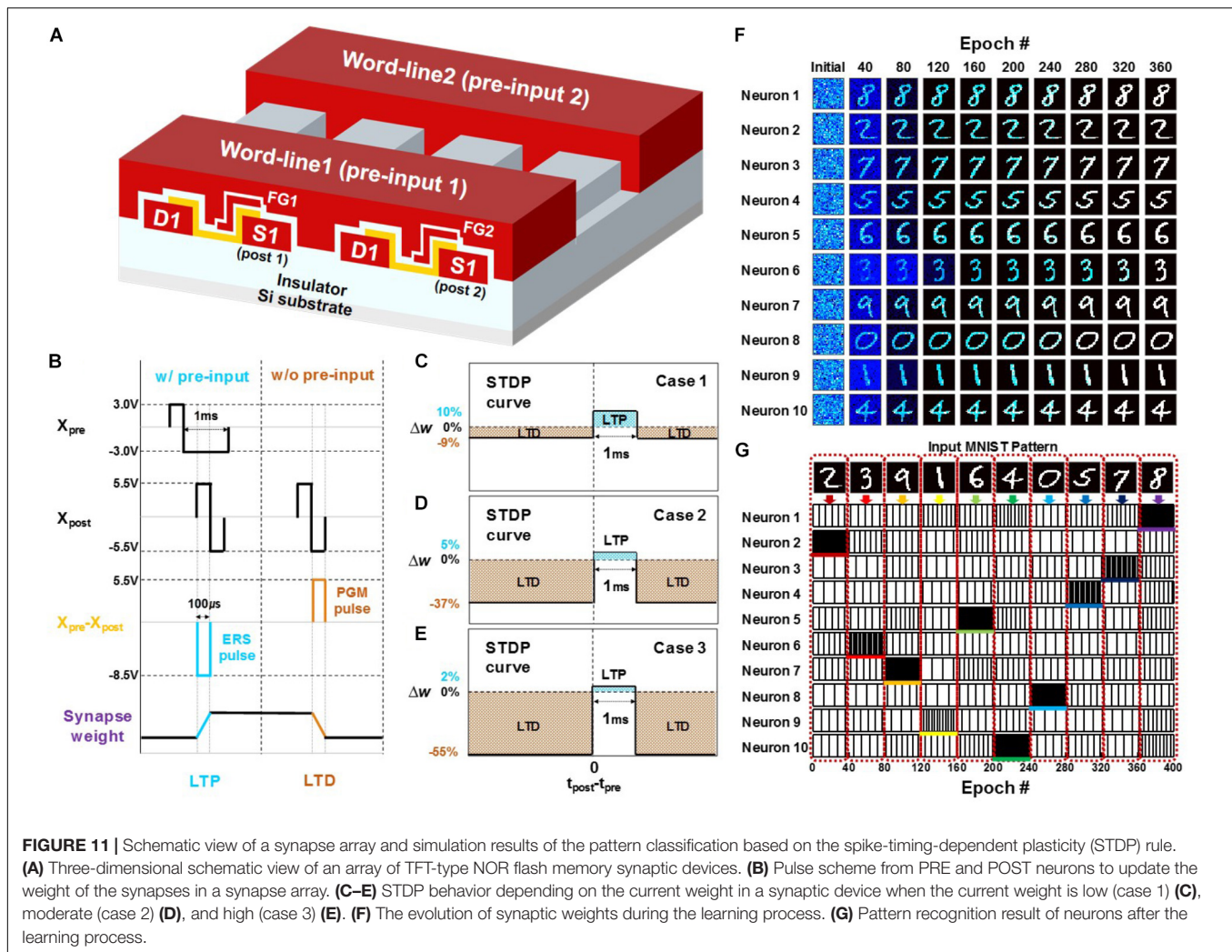
We perform a simulation to compare the energy consumption of three different neuron circuits shown in **Figures 9A–C**. They are the PF neuron, an I&F circuit using a conventional MOSFET with a charge trap layer (MOS neuron), and a conventional I&F circuit with a C_{mem} (conventional neuron). In the PF neuron (or MOS neuron), as the signal from the synapses is transferred to the charge trap layer, the $V_{on,PF}$ (or $V_{on,MOS}$) decreases gradually. A spike is generated when $V_{on,PF}$ (or $V_{on,MOS}$) is lower than V_{read} , which means that the neuron fires. On the other hand, in the conventional neuron, the signal from the synapses is integrated into the C_{mem} , resulting in a change in the membrane potential (V_{mem}). If V_{mem} exceeds a certain threshold (V_{th}) in conventional neuron, a spike is generated. **Figure 9D** shows the transient currents before firing when the same number of input pulses are given to the three different neuron circuits. Here, for precise comparisons, $V_{on,PF}$, $V_{on,MOS}$, or V_{mem} changes by 8 mV for each pulse from the synapses, and all neurons are set to generate a spike when 25 pulses are applied. The energies consumed per spike in the conventional neuron and MOS neuron are 25 pJ/spike and 12.5 pJ/spike, respectively. In contrast, the energy consumption per spike in the PF neuron is only 0.25 pJ/spike due to the super-steep SS (0.04 mV/dec) of the proposed PF device. For reference, the SS of the devices that trigger spike generation in the conventional neuron and MOS neuron is above 60 mV/dec at room temperature. The dotted circle in each neuron represents the trigger device. The trigger device in the PF neuron is the PF device. Note that in



the conventional neuron, if V_{mem} slowly increases to V_{th} or stays at a voltage slightly lower than V_{th} , the energy consumption is greatly increased because the subthreshold current flows through

the trigger device. It should be noted that the same situation also occurs in the MOS neuron. In the proposed PF device, however, the subthreshold current at a lower voltage than the $V_{on,PF}$ is





negligibly small, which greatly reduces the energy consumption. Moreover, the PF neuron has a foot print of about $52F^2$ except for the self-controller, thereby reducing the neuron area by about 17 times compared with that of the conventional neuron ($\sim 866F^2$) with a large C_{mem} .

Multiple Neuron System

Figure 10A shows a crossbar architecture with a common self-controller in a neuron layer. Here, PF neurons and synaptic devices are depicted by the dots and squares, respectively. As in the conventional model of the crossbar layout, input and output neurons are connected by the synaptic devices in a feed-forward manner. Synaptic devices receive a spike signal from the input neurons, and the output neuron receives the signal corresponding to the weighted sum of the synaptic devices. Many neurons in a neuron layer share one common self-controller as depicted by the green box at the top center of **Figure 10A**. **Figure 10B** shows a detailed schematic diagram of a multiple neuron system in a neuron layer depicted by a dashed line in **Figure 10A**. When a spike signal from a fired PF neuron is transmitted into the common self-controller, it generates reset, lateral inhibition, and

N1 control pulses. By the switch control unit, reset and lateral inhibition pulses are sent to the fired neuron and remaining neurons except for the fired neuron in the same neuron layer, respectively. The reset pulse returns the PF device in the fired neuron to its initial state, and the lateral inhibition pulse reduces the possibility of firing the remaining neurons to some extent. Note that a positive inhibition pulse is used in our circuit, and its magnitude is designed to be smaller than that of the reset pulse (see **Figures 10G–I**). Additionally, the N1 control pulse is sent to the N1 devices of all the PF neurons, temporarily turning off the N1 devices (**Figure 8A**). Note that by using only one common self-controller in a neuron layer to perform the various functions, the number of transistors in each PF neuron decreases, resulting in high integration density of the neurons.

Transient multiple neurons behaviors in a neuron layer were verified by a circuit simulator as follows. Whenever a PF neuron fires (**Figure 10J**), an N1 control pulse is applied to all neurons to turn off the N1 devices shown in **Figure 10F**. Then, the reset pulse with an amplitude of 10 V is applied to the fired PF neuron, and the lateral inhibition pulse with an amplitude of 7 V is applied to the PF neurons except for the fired neuron shown

in **Figures 10G–I**. **Figures 10C–E** show examples of the three pulse sequences from the synapses, respectively. Each pulse train is applied to the PF device of each neuron. Here, positive pulses in each voltage pulse train represent reset (10 V) or inhibition (7 V) pulses transmitted from the self-controller whenever a neuron fires.

Demonstration of the PF Neuron in a Neural Network

To verify the feasibility of the PF neuron at the network level, on-line unsupervised pattern learning and recognition were investigated in a SNN based on the PF neuron. A fully connected 2-layer SNN system consisting of an input layer of 784 presynaptic neurons and an output layer of 10 postsynaptic neurons was constructed. The pattern classification was performed using a MATLAB simulator. For the simulation, the characteristics of a TFT-type NOR flash memory synaptic device in our previous work (Kim et al., 2018) were adopted for its high performance in a neural network. **Figure 11A** shows a three-dimensional schematic view of an array of TFT-type NOR flash memory synaptic devices. Input signals from presynaptic neurons and a feedback spike pulse from the self-controller in the postsynaptic neuron layer are applied to the word-lines (WLs) and the source, respectively, to perform a long-term potentiation (LTP) and a long-term depression (LTD) by the erasing and programming of the memory cell. The pulse scheme used for the synaptic weight update is shown in **Figure 11B**. When a postsynaptic neuron fires, the weights of the synapse cells to which the input signals are applied are potentiated, and the weights of the other cells without input signals are depressed. The STDP curves derived from the measured LTP/LTD characteristics of the synaptic device by using the pulse scheme are shown in **Figures 11C–E**. **Figure 11C** shows the shape of the STDP curve when the synaptic weight is low. **Figures 11D,E** show the shapes of the STDP curve when the weight of the synapse is moderate and high, respectively.

Pattern classification simulation using the synapse array and the PF neurons is explained as follows. Here, ten binary 28×28 input patterns using the MNIST handwritten patterns of the digits 0–9 are used for both learning and recognition. As the input signals of ten MNIST digits are randomly applied to the 784 presynaptic neurons, a postsynaptic neuron of 10 postsynaptic neurons fires by the weighted sum of the synapses, and the weights of synapses in the synapse array connected to the fired postsynaptic neuron are updated by the STDP learning rule. To prevent the co-specialization of postsynaptic neurons, a lateral inhibition function is used by applying the lateral inhibition pulse to all postsynaptic neurons except for the fired postsynaptic neuron. As the unlabeled binary 28×28 input patterns are repeatedly presented to the synapse array, each postsynaptic neuron is gradually trained to a specific pattern shown in **Figure 11F**. After the learning process, a recognition test is carried out by randomly presenting the input patterns used in the learning process. Each postsynaptic neuron fires differently in response to each specific pattern shown in **Figure 11G**. The

input patterns are recognized by comparing the firing rate of the postsynaptic neurons between 10 postsynaptic neurons resulting in the successful classification of ten MNIST pattern images in an unsupervised learning manner. These simulation results show that the neural network based on our PF neuron successfully performs on-line unsupervised pattern learning and recognition.

CONCLUSION

We have demonstrated the I&F function of biological neurons using the proposed body-floated PF device, fabricated on the same wafer with body-connected CMOS FETs for high a performance neuron circuit. The SS obtained from the fabricated PF device was excellent at 0.04 mV/dec due to the PF in the switching, resulting in a low energy consumption of ~ 0.25 pJ per spike of the neuron circuit using the PF device. The energy consumption is about 100 times less than that of the conventional neuron circuit. The PF neuron area was reduced by about 17 times compared to that of the conventional neuron by replacing a large C_{mem} in the conventional neuron to the charge trap layer of the PF device keeping the integrate function of biological neurons. Furthermore, the high density multiple neuron system with reset and lateral inhibition functions was demonstrated through simulation by using only one common self-controller in a neuron layer. We have successfully verified the on-line unsupervised pattern learning and recognition in the SNN system using our PF devices and the synaptic devices. These results show the feasibility of a hardware-based implementation of energy-efficient and high-density analog computing using our PF device.

AUTHOR CONTRIBUTIONS

KB, SW, and JH conceived and designed the experiments. KB and SW built the devices and carried out the measurements. KB, SW, and WM performed the circuit simulation. SOL, CH, and SUL performed the pattern learning and recognition simulation. KB, SW, WM, SOL, CH, JH, SUL, and JH performed the theoretical analyses. KB, SW, WM, SOL, CH, and JH wrote the manuscript. All authors discussed the results and commented on the manuscript.

FUNDING

This work was supported by the National Research Foundation of Korea (NRF- 2016M3A7B4909604) and the Brain Korea 21 Plus Project in 2018.

SUPPLEMENTARY MATERIAL

The Supplementary Material for this article can be found online at: <https://www.frontiersin.org/articles/10.3389/fnins.2018.00704/full#supplementary-material>

REFERENCES

- Abele, N., Fritsch, R., Boucart, K., Casset, F., Ancey, P., and Ionescu, A. M. (2005). "Suspended-Gate MOSFET: bringing new MEMS functionality into solid-state MOS transistor," in *Technical Digest - International Electron Devices Meeting*, Washington, DC, 1–3. doi: 10.1109/IEDM.2005.1609384
- Basu, A., Shuo, S., Zhou, H., Lim, M. H., and Huang, G.-B. (2013). Silicon spiking neurons for hardware implementation of extreme learning machines. *Neurocomputing* 102, 125–134. doi: 10.1016/j.neucom.2012.01.042
- Cantley, K. D., Subramaniam, A., Stiegler, H. J., Chapman, R. A., and Vogel, E. M. (2011). Hebbian learning in spiking neural networks with nanocrystalline silicon TFTs and memristive synapses. *IEEE Trans. Nanotechnol.* 10, 1066–1073. doi: 10.1109/TNANO.2011.2105887
- Chen, Y.-H., Krishna, T., Emer, J. S., and Sze, V. (2017). Eyeriss: an energy-efficient reconfigurable accelerator for deep convolutional neural networks. *IEEE J. Solid State Circuits* 52, 127–138. doi: 10.1109/JSSC.2016.2616357
- Cheung, K. P. (2010). "On the 60 mV/dec @300 K limit for MOSFET subthreshold swing," in *International Symposium VLSI Technology System Applications (VLSI-TSA)*, Taiwan, 72–73. doi: 10.1109/VTSA.2010.5488941
- Chicca, E., Stefanini, F., Bartolozzi, C., and Indiveri, G. (2014). Neuromorphic electronic circuits for building autonomous cognitive systems. *Proc. IEEE* 102, 1367–1388. doi: 10.1109/JPROC.2014.2313954
- Choi, W. Y., Park, B.-G., Lee, J. D., and Liu, T.-J. K. (2007). Tunneling field-effect transistors (TFETs) with subthreshold swing (SS) less than 60 mV/dec. *IEEE Electron Device Lett.* 28, 743–745. doi: 10.1109/LED.2007.901273
- Choi, W. Y., Song, J. Y., Lee, J. D., Park, Y. J., and Park, B.-G. (2005). "70-nm impact-ionization metal-oxide-semiconductor (I-MOS) devices integrated with tunneling field-effect transistors (TFETs)," in *Technical Digest - International Electron Devices Meeting*, Washington, DC, 1–4. doi: 10.1109/IEDM.2005.1609519
- Dirani, H. E., Fonteneau, P., Solaro, Y., Legrand, C.-A., Marin-Cudraz, D., Ferrari, P., et al. (2017). Sharp-switching band-modulation back-gated devices in advanced FDSOI technology. *Solid State Electron.* 128, 180–186. doi: 10.1016/j.sse.2016.10.008
- Dirani, H. E., Solaro, Y., Fonteneau, P., Ferrari, P., and Cristoloveanu, S. (2016). Properties and mechanisms of Z2-FET at variable temperature. *Solid State Electron.* 115, 201–206. doi: 10.1016/j.sse.2015.08.015
- Dutta, S., Kumar, V., Shukla, A., Mohapatra, N. R., and Ganguly, U. (2017). Leaky integrate and fire neuron by charge-discharge dynamics in floating-body MOSFET. *Sci. Rep.* 7:8257. doi: 10.1038/s41598-017-07418-y
- Eryilmaz, S. B., Kuzum, D., Yu, S., and Philip Wong, H.-S. (2015). "Device and system level design considerations for analog-non-volatile-memory based neuromorphic architectures," in *IEEE International Electron Devices Meeting*, San Francisco, CA, 64–67. doi: 10.1109/IEDM.2015.7409622
- Ghosh-Dastidar, S., and Adeli, H. (2009). Spiking neural networks. *Int. J. Neural Syst.* 19, 295–308. doi: 10.1142/S0129065709002002
- Hinton, G. E., Osindero, S., and Teh, Y.-W. (2006). A fast learning algorithm for deep belief nets. *Neural Comput.* 18, 1527–1554. doi: 10.1162/neco.2006.18.7.1527
- Indiveri, G., Linares-Barranco, B., Hamilton, T. J., Schaik, A. V., Etienne-Cummings, R., Delbruck, T., et al. (2011). Neuromorphic silicon neuron circuits. *Front. Neurosci.* 5:73. doi: 10.3389/fnins.2011.00073
- Jeon, Y., Kim, M., Lim, D., and Kim, S. (2015). Steep subthreshold swing n- and p-channel operation of bendable feedback field-effect transistors with p + -i-n + nanowires by dual-top-gate voltage modulation. *Nano Lett.* 15, 4905–4913. doi: 10.1021/acs.nanolett.5b00606
- Jo, J., Choi, W. Y., Park, J.-D., Shim, J. W., Yu, H.-Y., and Shin, C. (2015). Negative capacitance in organic/ferroelectric capacitor to implement steep switching MOS devices. *Nano Lett.* 15, 4553–4556. doi: 10.1021/acs.nanolett.5b01130
- Kasabov, N. K. (2014). NeuCube: a spiking neural network architecture for mapping, learning and understanding of spatio-temporal brain data. *Neural Netw.* 52, 62–76. doi: 10.1016/j.neunet.2014.01.006
- Kim, C.-H., Lee, S., Woo, S. Y., Kang, W.-M., Lim, S., Bae, J.-H., et al. (2018). Demonstration of unsupervised learning with spike-timing-dependent plasticity using a TFT-type NOR flash memory array. *IEEE Trans. Electron Devices* 65, 1774–1780. doi: 10.1109/TED.2018.2817266
- Kim, S., Ishii, M., Lewis, S., Perri, T., BrightSky, M., Kim, W., et al. (2015). "NVM neuromorphic core with 64k-cell (256-by-256) phase change memory synaptic array with on-chip neuron circuits for continuous in-situ learning," in *IEEE International Electron Devices Meeting*, San Francisco, CA, 443–446. doi: 10.1109/IEDM.2015.7409716
- Krizhevsky, A., Sutskever, I., and Hinton, G. E. (2017). imagenet classification with deep convolutional neural networks. *Commun. ACM* 60, 84–90. doi: 10.1145/3065386
- LeCun, Y., Bengio, Y., and Hinton, G. (2015). Deep learning. *Nature* 521, 436–444. doi: 10.1038/nature14539
- Liu, Y., Fan, Y., and Chen, J. (2017). Flame images for oxygen content prediction of combustion systems using DBN. *Energy Fuels* 13, 1445–1454. doi: 10.1021/acs.energyfuels.7b00576
- Livi, P., and Indiveri, G. (2009). "A current-mode conductance-based silicon neuron for address-event neuromorphic systems," in *IEEE International Symposium on Circuits and Systems*, Hokkaido, 2898–2901. doi: 10.1109/ISCAS.2009.5118408
- Moon, K., Cha, E., Park, J., Gi, S., Chu, M., Baek, K., et al. (2015). "High density neuromorphic system with Mo/Pr_{0.7}Ca_{0.3}MnO₃ synapse and NbO₂ IMT oscillator neuron," in *IEEE International Electron Devices Meeting*, San Francisco, CA, 463–466. doi: 10.1109/IEDM.2015.7409721
- Ostwal, V., Meshram, R., Rajendran, B., and Ganguly, U. (2015). "An Ultra-compact and Low Power Neuron based on SOI platform," in *International Symposium VLSI Technology System Applications (VLSI-TSA)*, Taiwan, 1–2. doi: 10.1109/VLSI-TSA.2015.7117569
- Park, S., Noh, J., Choo, M. L., Sheri, A. M., Chang, M., Kim, Y.-B., et al. (2013). Nanoscale RRAM-based synaptic electronics: toward a neuromorphic computing device. *Nanotechnology* 24:384009. doi: 10.1088/0957-4484/24/38/384009
- Park, Y., and Lee, J.-S. (2017). Artificial synapses with short- and long-term memory for spiking neural networks based on renewable materials. *ACS Nano* 11, 8962–8969. doi: 10.1021/acsnano.7b03347
- Pouyan, P., Amat, E., and Rubio, A. (2014). "Reliability challenges in design of memristive memories," in *5th European Workshop on CMOS Variability (VARI)*, Palma de Mallorca, 1–6. doi: 10.1109/VARI.2014.6957074
- Qiao, N., Mostafa, H., Corradi, F., Osswald, M., Stefanini, F., Sumislawska, D., et al. (2015). A reconfigurable on-line learning spiking neuromorphic processor comprising 256 neurons and 128K synapses. *Front. Neurosci.* 9:141. doi: 10.3389/fnins.2015.00141
- Rajendran, B., Liu, Y., Seo, J.-S., Gopalakrishnan, K., Chang, L., Friedman, D. J., et al. (2013). Specifications of nanoscale devices and circuits for neuromorphic computational systems. *IEEE Trans. Electron Devices* 60, 246–253. doi: 10.1109/TED.2012.2227969
- Sharad, M., Augustine, C., Panagopoulos, G., and Roy, K. (2012). "Spin-based neuron model with domain-wall magnets as synapse," in *IEEE Transactions Nanotechnol.*, Vol. 11, Portland, OR, 843–853. doi: 10.1109/TNANO.2012.2202125
- Su, L. T., Chung, J. E., Antoniadis, D. A., Goodson, K. E., and Flik, M. I. (1994). Measurement and modeling of self-heating in SOI NMOSFET's. *IEEE Trans. Electron Devices* 41, 69–75. doi: 10.1109/16.259622
- Turaga, S. C., Murray, J. F., Jain, V., Roth, F., Helmstaedter, M., Briggman, K., et al. (2010). Convolutional networks can learn to generate affinity graphs for image segmentation. *Neural Comput.* 22, 511–538. doi: 10.1162/neco.2009.10-08-881
- Vandana, B. (2013). Study of floating body effect in SOI technology. *Int. J. Mod. Eng. Res.* 3, 1817–1824.
- Wan, J., Cristoloveanu, S., Royer, C. L., and Zaslavsky, A. (2012). A feedback silicon-on-insulator steep switching device with gate-controlled carrier injection. *Solid State Electron.* 76, 109–111. doi: 10.1016/j.sse.2012.05.061
- Wan, J., Royer, C. L., Zaslavsky, A., and Cristoloveanu, S. (2013). A systematic study of the sharp-switching Z2-FET device: from mechanism to modeling and compact memory applications. *Solid State Electron.* 90, 2–11. doi: 10.1016/j.sse.2013.02.060
- Wang, Z., Joshi, S., Savel'ev, S., Song, W., Midya, R., Li, Y., et al. (2018). Fully memristive neural networks for pattern classification with unsupervised learning. *Nat. Electron* 1, 137–145. doi: 10.1038/s41928-018-0023-2
- Wijekoon, J. H. B., and Dudek, P. (2008). Compact silicon neuron circuit with spiking and bursting behavior. *Neural Netw.* 21, 524–534. doi: 10.1016/j.neunet.2007.12.037

- Wu, C.-C., Wu, W.-F., Su, P. Y., Chen, L. J., and Ko, F.-H. (2007). Effects of capping layer on the electrical characteristics of nickel silicided junctions. *Microelectron. Eng.* 84, 1801–1805. doi: 10.1016/j.mee.2007.01.198
- Yu, S., Wu, Y., Jeyasingh, R., Kuzum, D., and Philip Wong, H.-S. (2011). An electronic synapse device based on metal oxide resistive switching memory for neuromorphic computation. *IEEE Trans. Electron Devices* 58, 2729–2737. doi: 10.1109/TED.2011.2147791
- Zhang, D., Zeng, L., Cao, K., Wang, M., Peng, S., Zhang, Y., et al. (2016). “All spin artificial neural networks based on compound spintronic synapse and neuron,” in *IEEE Transactions on Biomedical Circuits and Systems*, Vol. 10, (Beihang: Beihang University), 828–836. doi: 10.1109/TBCAS.2016.2533798

Conflict of Interest Statement: The authors declare that the research was conducted in the absence of any commercial or financial relationships that could be construed as a potential conflict of interest.

The reviewer NM and handling Editor declared their shared affiliation.

Copyright © 2018 Choi, Woo, Kang, Lee, Kim, Bae, Lim and Lee. This is an open-access article distributed under the terms of the Creative Commons Attribution License (CC BY). The use, distribution or reproduction in other forums is permitted, provided the original author(s) and the copyright owner(s) are credited and that the original publication in this journal is cited, in accordance with accepted academic practice. No use, distribution or reproduction is permitted which does not comply with these terms.